NRC·CNRC

NRC Publications Archive
Archives des publications du CNRC

Editors' choice—optical emission from germanium nanocrystals
Rowell, N. L.; Lockwood, D. J.; Houghton, D. C.; Noël, J.-P.; Baribeau, J.-M.

This publication could be one of several versions: author's original, accepted manuscript or the publisher's version. / La version de cette publication peut être l'une des suivantes : la version prépublication de l'auteur, la version acceptée du manuscrit ou la version de l'éditeur.
For the publisher's version, please access the DOI link below./ Pour consulter la version de l'éditeur, utilisez le lien DOI ci-dessous.

Publisher's version / Version de l'éditeur:
https://doi.org/10.1149/2.0041812jss
ECS Journal of Solid State Science and Technology, 7, 12, pp. R195-R205, 2018-11-29

NRC Publications Archive Record / Notice des Archives des publications du CNRC :
https://nrc-publications.canada.ca/eng/view/object/?id=0ef78934-9319-4bd4-a136-85f0bebdea9f
https://publications-cnrc.canada.ca/fra/voir/objet/?id=0ef78934-9319-4bd4-a136-85f0bebdea9f

Access and use of this website and the material on it are subject to the Terms and Conditions set forth at
https://nrc-publications.canada.ca/eng/copyright
READ THESE TERMS AND CONDITIONS CAREFULLY BEFORE USING THIS WEBSITE.

L'accès à ce site Web et l'utilisation de son contenu sont assujettis aux conditions présentées dans le site
https://publications-cnrc.canada.ca/fra/droits
LISEZ CES CONDITIONS ATTENTIVEMENT AVANT D'UTILISER CE SITE WEB.

Questions? Contact the NRC Publications Archive team at
PublicationsArchive-ArchivesPublications@nrc-cnrc.gc.ca. If you wish to email the authors directly, please see the first page of the publication for their contact information.

Vous avez des questions? Nous pouvons vous aider. Pour communiquer directement avec un auteur, consultez la première page de la revue dans laquelle son article a été publié afin de trouver ses coordonnées. Si vous n'arrivez pas à les repérer, communiquez avec nous à PublicationsArchive-ArchivesPublications@nrc-cnrc.gc.ca.

National Research Council Canada
Conseil national de recherches Canada

ECS Journal of Solid State
Science and Technology

OPEN ACCESS

Editors' Choice—Optical Emission from Germanium Nanocrystals

To cite this article: N. L. Rowell *et al* 2018 *ECS J. Solid State Sci. Technol.* **7** R195

View the article online for updates and enhancements.

This content was downloaded from IP address 167.37.63.9 on 16/06/2020 at 23:12

Optical Emission from Germanium Nanocrystals

N. L. Rowell,[z] D. J. Lockwood,[*] D. C. Houghton, J.-P. Noël, and J.-M. Baribeau

National Research Council, Ottawa, Ontario K1A 0R6, Canada

We analyze the intense photoluminescence (PL) observed at energies from 600 to 1100 meV for a large number of $Si_{1-x}Ge_x$ epitaxial layers grown by molecular beam epitaxy. In the present work we show that this previously unexplained broad PL peak can be assigned to Ge nanocrystals (NCs) self-assembled within the SiGe layers. These NCs are assumed to be lattice matched to the SiGe in the vertical, growth direction. A consequence of this assignment is that as the Ge-fraction in the SiGe layer increases the vertical strain in the NCs changes from compressive to tensile at x ∼ 0.36, lowering the NC bandgap (BG) below that of bulk Ge. We examine the PL results for more than 60 samples exhibiting this broad PL peak by examining how it follows the strained Ge BG for x from 0.05 to 0.53. The PL is resolvable as two narrower peaks separated by the momentum conserving phonon energy for Ge. Strain and confinement shifted NC bound exciton energies calculated numerically agree well with the measured ones. When Raman scattering results were examined for some of the same samples, the phonon mode frequencies obtained provided valuable corroborative evidence for the presence of the Ge NCs.

© The Author(s) 2018. Published by ECS. This is an open access article distributed under the terms of the Creative Commons Attribution 4.0 License (CC BY, http://creativecommons.org/licenses/by/4.0/), which permits unrestricted reuse of the work in any medium, provided the original work is properly cited. [DOI: 10.1149/2.0041812jss]

Manuscript submitted October 16, 2018; revised manuscript received November 16, 2018. Published November 29, 2018.

A silicon-compatible group IV coherent light source remains the missing link in Si-based photonics, despite the great variety of approaches explored; e.g., carrier localization, rare-earth doping, and stimulated light scattering. Although achieving efficient light emission from group IV semiconducting materials–a subject of intense research activity–has proven elusive, carrier localization methods have led to significantly enhanced optical emission from indirect gap materials and, notably, at higher temperatures. For example, room-temperature visible photoluminescence (PL) has been observed from porous Si[1] and strong infrared PL from various island or quantum dot systems.[2–9] A particular focus has been the study of self-organized structures containing nanometer sized Si[10] and Ge crystals,[11] which being compatible with present Si technology have important capabilities for device engineering. Applications include those in optoelectronics,[12] tunneling devices,[13–15] and nanocrystal memories.[10,16] Recently, lasing or very high efficiency PL has been shown for Ge, a material with a relatively small indirect to direct bandgap (BG) difference, which can be overcome with tensile strain and/or high doping,[17–21] or by alloying with tin.[22]

Previously[23] we have observed a very intense, low temperature PL with a large lifetime in dozens of our samples for molecular beam epitaxy (MBE)-grown $Si_{1-x}Ge_x$ epitaxial layers with x ranging from 0.05 to 0.53. Efficiencies in the 5% range – unheard of for group IV materials – were observed. This PL was neither defect nor dislocation related, and was suspected to be due to carrier localization effects. Here, we show that the PL is characteristic of self-assembled Ge nanocrystals (NCs) contained within the alloy epilayers through a thorough investigation of its concentration dependence both experimentally and theoretically. The presence of these strained Ge NCs is confirmed through Raman measurements.

Experimental

Although the present work is largely an interpretation of previously obtained data, a brief description follows as to how the samples in question were grown and their PL[23] and Raman properties were measured. The growth of the material was by conventional, solid source MBE without intentional doping in an ultrahigh vacuum deposition chamber. The growth temperature was measured with an optical pyrometer in the range 350–900°C. The Si growth rate was 1 Å/s and the Ge growth rate was set to achieve a given value of x. The single or multiple quantum well structures were designed to be stable with respect to misfit strain relaxation.[24]

*Electrochemical Society Fellow.

zE-mail: nelson.rowell@nrc-cnrc.gc.ca

The PL spectra were measured using a Bomem DA3 FTIR spectrometer with samples at liquid helium temperatures, excited with 1 to 400 mW of either 457.9, 488.0, or 514.5 nm laser light from an argon ion laser. Varying the wavelength of the exciting light affected the depth of penetration into the sample. The advantages of using a Fourier transform spectrometer for PL studies are well known.[25] A radiometric calibration was performed to obtain the relative spectral responsivity of the system from 500 to 1400 meV, which was used to normalize the raw spectral data. Especially important in these measurements were the ultra-sensitive detectors used, which were comprised of an Applied Detectors Corporation Ge PIN photodiode for the range from 700 to 1200 meV and a cold-filtered Cincinnati Electronics InSb photodiode for the range from 500 to 1000 meV.

The Raman spectra of the various samples were recorded at room temperature in a quasi-backscattering geometry[26] using 300 mW of argon laser light at 457.9 nm for excitation with the exception of sample 648 (x = 0.258) where ∼150 mW of krypton laser light at 468.0 nm was used. With these blue laser lines the penetration depth of the exciting light[26] is more comparable to the superlattice or epilayer overall thickness. This minimizes the Raman contribution from the Si substrate, but not that from the Si layers in superlattices. The incident light polarization (along the Y direction external to the sample) was in the plane of the incident light (along X) and the light scattered at 90° to the incident light (along Y), and was recorded without polarization analysis. Under these conditions, the light scattering polarization in the orthogonal laboratory coordinate system is X(YZ + YX)Y, which corresponds closely to $z(y'x' + y'y')\bar{z}$ polarization within the sample, where z is the sample growth direction (along the cubic Si substrate c axis, say) and x' and y' are at 45° to the crystal a and b axes, respectively. The scattered light was analyzed with a Spex 14018 double monochromator, detected with a cooled RCA 31034A photomultiplier, and recorded under computer control. The spectral resolution was 3.1 ± 0.1 cm^{-1} for all samples except the x = 0.258 sample where it was 2.9 ± 0.1 cm^{-1}. All measurements were carried out at 295 K in a helium-gas atmosphere, which was used to help cool the sample and also to eliminate air features from the Raman spectrum.

Results and Discussion

Photoluminescence of Germanium: bulk.—As Ge is thought to be the material forming the NCs that give rise to the broad PL, it is useful to review the PL properties of bulk Ge.[25,27–32] In general the PL spectrum for bulk Ge resembles that of bulk Si with NP lines of varying strengths and relatively stronger phonon replica lines. There are, however, some notable differences between Si and Ge PL. In particular the longitudinal acoustic (LA) phonon replica (PR) is (by

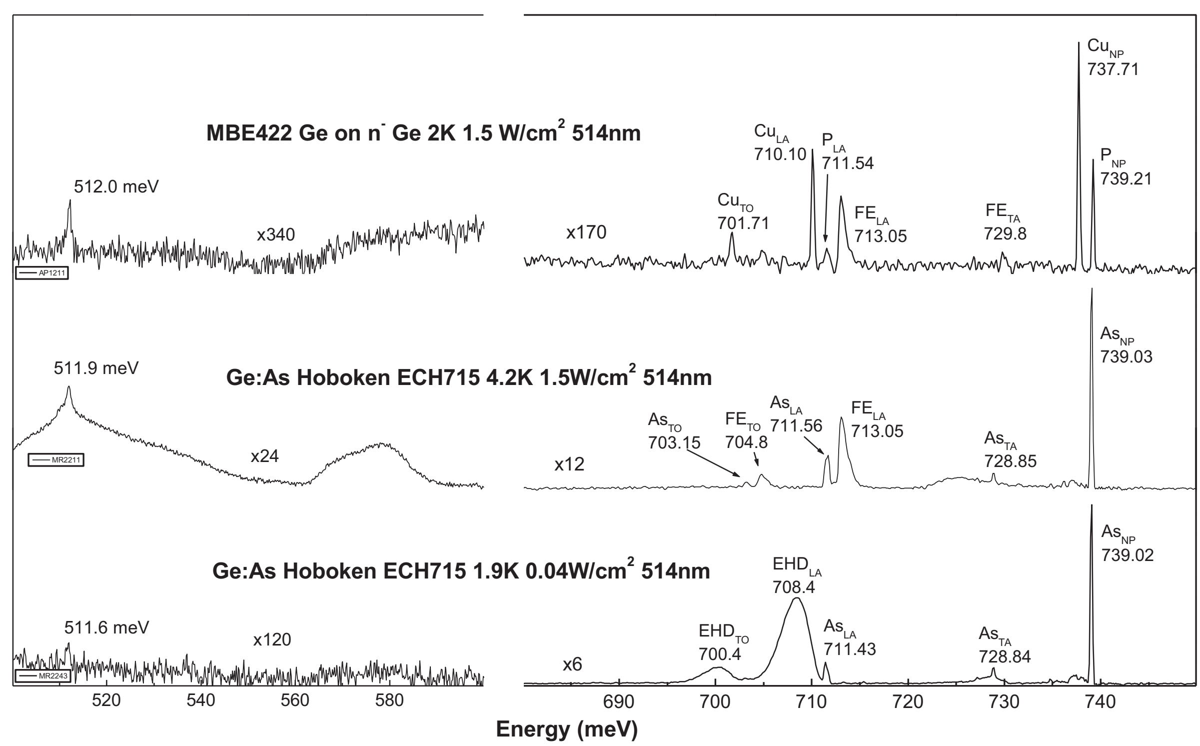

Figure 1. PL spectra with 514 nm excitation for two different Ge samples at various excitation powers and temperatures.

a considerable margin) the stronger replica, electron-hole droplets (EHDs)[33] form readily (especially at lower temperatures and higher excitation densities), and Ge has more prominent isotope effects in PL.[34]

The PL spectra with 514 nm excitation over an area of 0.1 cm^2 are shown in Figure 1 for two different Ge samples. Literature values for no-phonon (NP) bound exciton (BE) energies include 739.22 meV for phosphorus and 739.08 meV for arsenic.[28,35] The trace in Figure 1 labeled MBE422 is that for a Ge epilayer sample grown by MBE on a n-type substrate (doped with phosphorus). This epilayer was apparently contaminated with copper as indicated by the Cu-related emission lines (NP at 737.7 meV).[36] The substrate for this

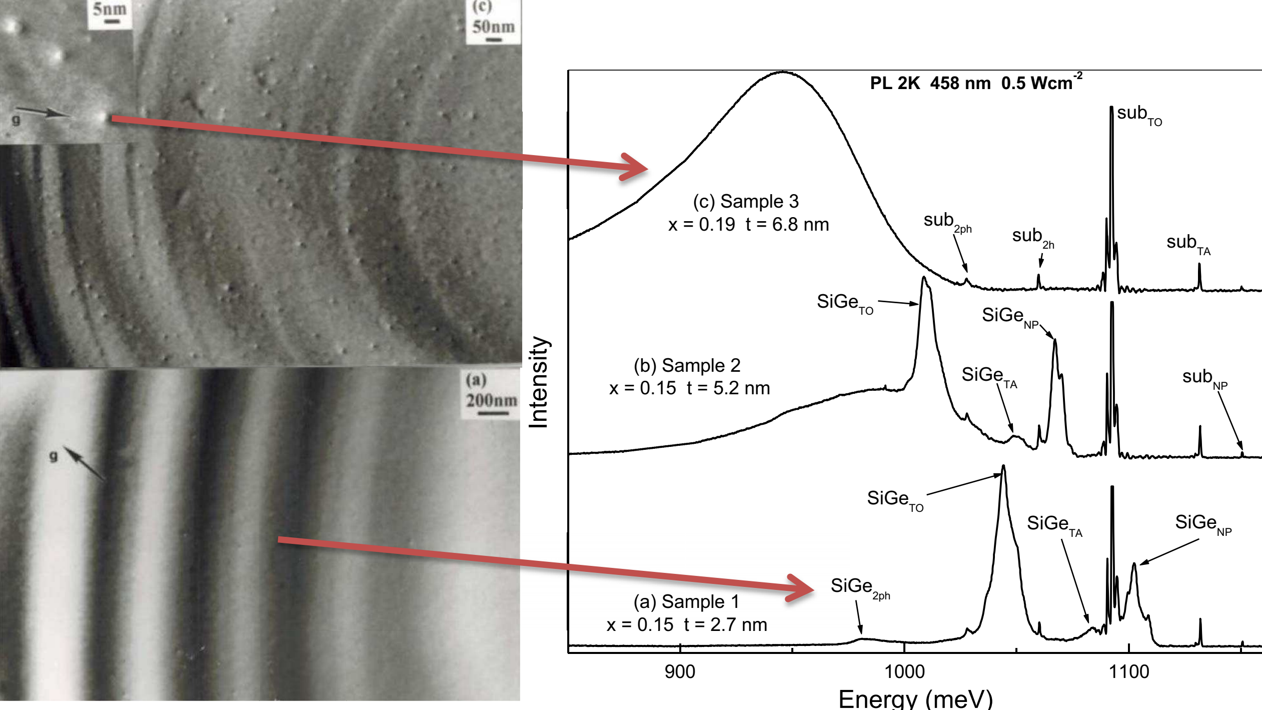

Figure 2. Phenomenology of the transition from PR to broad PL for three MBE $Si_{1-x}Ge_x$ multiple quantum well samples. The box on the right depicts the PL obtained from the three samples with essentially the same Ge fraction at 2 K, with the TEM pictures obtained from samples 1 and 3 shown on the left.

sample was phosphorus doped for which dopant the NP BE line is particularly strong at 739.21 meV. This MBE grown sample is the only pure Ge epilayer sample discussed here, and will not be included in the subsequent discussion of the SiGe samples. The sample labeled Hoboken (Umicore) was an As-doped, bulk sample (As at approximately 4×10^{14} cm^{-3}), which had a strong BE NP line near 739 meV, apparent in the lower two traces, which are from power densities varying from 1.5 at 4.2 K to 0.04 W/cm^2 at 1.9 K. The NP line for As doping is particularly strong compared with other dopants, in a manner similar to the behavior for silicon.[37] At lower temperatures, electron hole droplets (EHDs) were observed to predominate, exhibiting relatively wide emission lines several meV below the corresponding BE phonon replica lines. To lower energy, at about 512 meV, an impurity or defect line was seen near the line position often associated with Sn doping.[38] The EHD peaks shift with laser intensity and temperature. Their energies are several meV below the corresponding BE (or free exciton (FE)) phonon replicas, in approximately the same intensity ratios.

SiGe PL: phonon resolved and broad peak.—The PL spectra with broad peaks for more than 60 separate MBE growths were examined. Of these samples 30 had both broad and phonon resolved (PR) peaks in their spectra.

On the right of Figure 2 are the PL spectra for three $Si_{1-x}Ge_x$ multiple quantum well samples, each sample consisting of ten wells separated by Si spacers lattice matched in the x-y plane on Si (001) p-type substrates, with increasing well thickness from trace (a) to trace (c). The Ge fraction varied slightly from 0.15 for the two thinner well samples to 0.19 for the thicker well sample. On the left are the plan-view transmission electron microscope (TEM) images for two of the samples, one with the thinnest wells and the other with the thickest wells. The TEM images indicate the presence of small platelets of elevated Ge content for the thicker quantum wells. For trace (a), only phonon resolved PL lines are seen, both for the quantum wells and for the substrate, with the broader lines those associated with the quantum wells. The substrate lines are the NP line at 1150 meV, the TA PR line at 1130 meV, and the transverse optic (TO) PR around 1092 meV. The SiGe PL also consists primarily of a NP line and its TO replica, separated by the same Si-Si TO phonon frequency (58 meV) as for Si, although the NP line is relatively much stronger and wider, due to alloy disorder. The position of the SiGe NP line depends on the Ge fraction, hence the quantum well strain, and on the quantum well thickness through the confinement effect. When the well thickness is increased from 2.7 nm to 5.2 nm without changing the Ge fraction, the SiGe PR lines shift in tandem due to a reduction in the confinement shift for the thicker wells. We also see a rising broad background which peaks approximately 80 meV below the SiGe NP peak. For the thickest wells (c), the PR peaks are no longer present and an intense broad PL to lower photon energies dominates the spectrum.

In Figure 3 we see an example of a single sample which exhibits both broad and PR PL. For these low temperature PL spectra, the sample was comprised of three quantum wells with x = 0.17 and showed at various excitation intensities both the broad and phonon resolved (PR) PL as well as a feature due to the Si substrate (sub_{TO}). In that figure we see that at higher laser power densities the centers responsible for the broad PL become saturated and the PR peaks are more apparent. The main PR peaks are the NP peak associated with the SiGe BG and its TO PR, which are separated by 58 meV. The broad PL peak is approximately 100 meV lower in energy than the NP peak.

The $Si_{1-x}Ge_x$ well thickness and Ge fraction were determined using X-ray double-crystal diffraction and dynamical rocking curve analysis which yielded an absolute uncertainty in x of ± 0.02.[23] For samples exhibiting both broad and PR PL, the NP peak position in the PR spectrum was used as a separate indicator of layer thickness and Ge fraction (as in Figure 3).

As shown in Figure 3 and in Figure 4, the PL that we attribute to Ge NCs consists of a broad peak with an asymmetry to low photon energies. This peak displays little variation in shape with Ge fraction

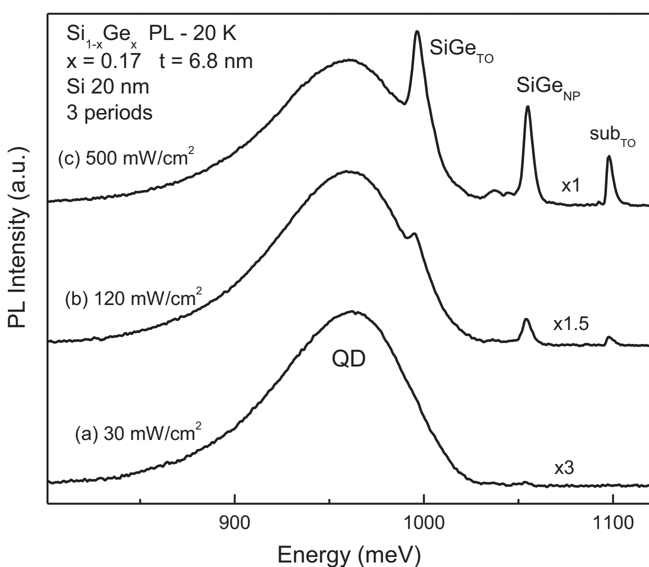

Figure 3. Low temperature PL spectra of a sample comprised of three quantum wells recorded under various excitation intensities, as indicated.

and tracks the BG variation, but is ∼100 meV below the indirect SiGe BG. If the material were Si or SiGe, the width of the peak at ∼ 50 meV would be too small for it to be due to a NP line with its TO PR, as the NP-TO spacing is about 58 meV for those materials. Figure 4 shows that for higher Ge fractions the PL is emitted at energies significantly below those for bulk Ge, with its indirect BG of 744 meV at low temperatures. The origin of the broad, intense PL peak has remained unexplained, until now. In Figure 4 we display low temperature PL from three SiGe samples and bulk Ge. For the spectrum in trace (a), the result is also illustrated with curve fitting using two Gaussian peaks for the broad PL peak. Table I contains comprehensive design and measured data for the SiGe alloy epitaxial samples grown by MBE that were used in this study. This table has ten columns: (1) sample number, (2) growth temperature in Celsius, (3 Ge fraction, (4) SiGe layer thickness, (5) number of periods, (6) Si spacer thickness,

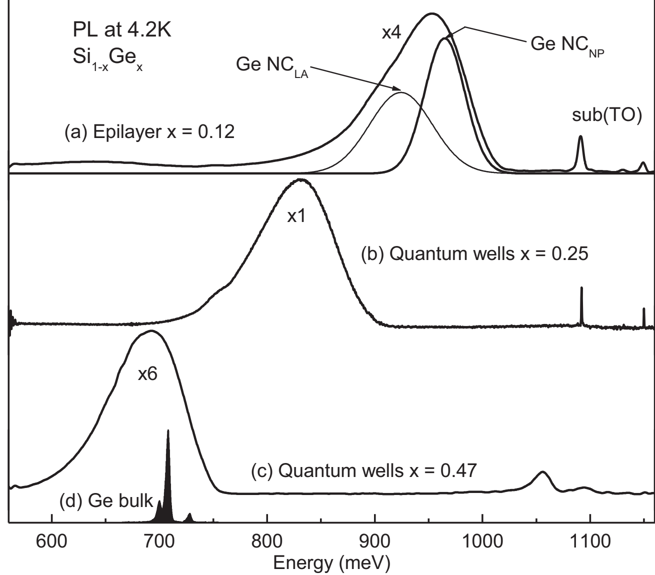

Figure 4. Low temperature PL from three SiGe samples and bulk Ge. For the spectrum in trace (a), the result is also illustrated with curve fitting using two Gaussian peaks for the broad PL peak.

Table I. SiGe alloy epitaxial samples grown by MBE that were used in this study. From left to right the columns contain (1) sample number, (2) growth temperature in Celsius, (3) Ge fraction, (4) SiGe layer thickness, (5) number of periods, (6) Si spacer thickness, (7) sample type, (8) PR NP line energy if present, (9) Energy of NC phonon peak, (10) Energy of NC NP peak. The latter two energies were obtained by fitting Gaussian functions to the broad PL peak (see Figure 4). The values for the Ge fraction and layer thicknesses are either the design values or values obtained with XRD measurement. The latter values are more precise and generally have more significant figures.

MBE#	Growth Temp. (C)	x	t_{SiGe} (A)	# Per.	t_{Si} (A)	Type	PL PR NP	PL Gauss1	PL Gauss2
1160	619	0.064	25.3	1		MQW	1130.8	1019.4	1047
1299	714	0.113	91	9	200	MQW	1049.2	940.9	978.1
894	500	0.12	1300	1		EPI		924.3	964.9
1167	595	0.146	26.7	20	200	MQW	1102.4	996.8	1031.9
1169	599	0.146	52	20	200	MQW	1067.2	961.6	1000.9
742	542	0.15	100	1		EPI		900.3	942
1115	523	0.15	200	1		EPI		917.1	961.2
1173	601	0.155	44.3	20	200	MQW	1057.7	962.7	996.7
1290	716	0.156	78.6	1		EPI	1055.1	934.8	969.1
1291	718	0.156	77.5	3	200	MQW	1053.4	952.7	971.6
1293	713	0.158	77.6	5	200	MQW		931.1	967.9
1292	710	0.158	80	7	200	MQW	1045.3	945.8	976.5
1175	501	0.159	70.2	15	200	MQW		939.4	974.7
1214	799	0.167	68	3	200	MQW	1054.7	929.5	967.5
346[a]	530	0.17	66	40	200	MQW		888.6	925.8
1217	809	0.17	116	2	200	MQW	1013	909.6	946.6
1244	792	0.17	60	3	200	MQW		937.9	971
1174	597	0.172	65.8	15	200	MQW	1032.7	935.9	967.4
1297	717	0.173	78.8	7	200	MQW	1044.8	915.2	957.3
869[a]	500	0.18	200	1		EPI		855.7	891
1176	435	0.187	64.1	15	200	MQW		924.3	959.6
1172	596	0.188	67.5	15	200	MQW		929.9	963.2
1218	618	0.2	60	3	200	MQW		925.5	959.9
1221	624	0.2	60	3	200	MQW		914.6	948.5
1222	789	0.2	60	3	200	MQW		908.8	945.1
1227	782	0.2	60	3	200	MQW	1053	952.8	986.6
1243	795	0.2	60	3	200	MQW	1010.6	902.7	935.5
1323	573	0.2	200	1		EPI	1040.6	924.3	958.5
1324	794	0.2	20,30,60	3	200	MQW	1097.1	947.3	981.7
1339	806	0.2	20,30,60	3	200	MQW		959.5	992
1367	781	0.2	20,30,60	3	200	MQW	1061.4	921.2	957.2
1368	779	0.2	20,30,60	3	15	MQW	1037.7	940.8	966.5
349[a]	530	0.25	76	40	200	MQW		809.6	841.4
648[a]	500	0.258	100	1		EPI		807.1	843.5
1191	601	0.273	42.3	1		EPI	980.6	880.3	914.1
613	550	0.28	100	1		EPI		788.4	824.8
951	707	0.28	500	1		EPI		805	839.5
1305	718	0.298	50	10	200	MQW	948.8	853.1	884.8
1306	724	0.299	50	10	200	MQW	943.9	847.5	873.5
1307	722	0.299	50	10	200	MQW	952.1	859.4	888.4
336	550	0.3	100	25	200	MQW		795.9	832
1187	597	0.3	45.8	1		EPI	959.6	854.5	887.4
1284	523	0.3	56	20	200	MQW		803.5	843.1
1482	550	0.36	49	10	114	MQW		800.1	831.8
1192	591	0.379	21.8	10	200	MQW		899.1	932.4
1194	600	0.401	40.3	10	200	MQW		803.7	835.5
926[a]	475	0.47	50	15	200	MQW		667.1	702.8
944	600	0.49	50	15	200	MQW		639.6	682.1
931[a]	475	0.53	50	15	200	MQW		614.8	671.6

[a]Sample also studied with Raman spectroscopy.

(7) sample type, (8) PR NP line energy if present, (9) Energy of NC phonon peak, (10) Energy of NC NP peak. The latter two energies were obtained by fitting Gaussian functions to the broad PL peak (see Figure 4). The values for the Ge fraction and layer thicknesses are either the design values or values obtained with XRD measurement. The latter values are more precise and generally have more significant figures.

The broad PL weakens with increasing temperature[23] but persists to approximately 100 K. The decay with temperature is nearly exponential as e^{-T/T_0} with T_0 approximately 30.1. With an indirect gap, the effective NC well depth is not sufficient to give emission at room temperature. However if enough tensile strain could be applied such that the direct gap was lower than the indirect one, higher temperature emission would be seen.

Ge NC phonon peaks.—As was shown in Figure 4a, the broad peak's width and asymmetric shape can be curve resolved into two symmetric peaks, separated by ∼35 meV, i.e., very near the momentum conserving TO phonon energy for Ge. The NP peak is wide (25–45 meV) due to NC confinement variations arising from size variability and to alloy disorder broadening in the SiGe. In Ge dots, we expect two main PL peaks, a NP line and a LA replica line, separated

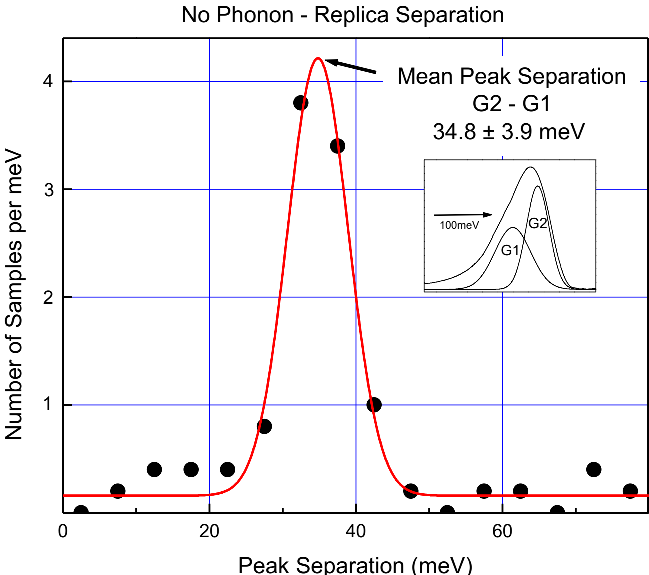

Figure 5. Number density for the PL samples versus the energy separation of the no phonon and phonon replica peaks, as evaluated using the curve fitting of two Gaussian peaks within the envelopes of the broad PL peaks (see inset).

by about 28 meV. So the NP-PR energies provided by curve resolving are relatively close to that (28 meV) for the most intense (LA) PR for Ge, but differ very significantly to the corresponding energy of the strongest (TO) PR for Si and SiGe, which, in both cases, is 58 meV. We also notice inhomogeneous broadening due to size effects and that the NP peak is relatively large, as would occur for a high degree of carrier localization in Ge NCs.

Shown in Figure 5 is a summary of the results from curve resolving two Gaussian peaks within the envelope of the broad PL peak, as illustrated in the inset. Here is shown the number of samples with peak separations within 5 meV of each other versus peak separation. For the samples studied here, the mean separation is 34.8 ± 3.9 meV, which is somewhat larger than the Ge LA phonon energy (28 meV) although very close to the Ge TO energy (33 meV). In the bulk, the dopant species has a strong effect on the ratios of the strengths of NP and PR lines. But in dots, doping is much less probable and the NP- PR ratios should be dominated by localization effects. (Dots disrupt the translational order in the crystal as do phonons, allowing for electron hole recombination without the emission of a phonon.).

The width of the NP line for dots suggests the range of their possible thicknesses. The width of the PR peak is complicated by the occurrence of multiple PRs although the LA replica is relatively strong compared to the TO and TA replicas, if their intensities are the same ratios for Ge NCs as for bulk Ge (several times to one from Hoboken material for both BE and EHD).

Raman results.—The samples investigated by Raman spectroscopy were numbers 346 ($x = 0.17$), 869 ($x = 0.18$), 349 ($x = 0.25$), 648 ($x = 0.258$), 926 ($x = 0.47$), and 931 ($x = 0.53$), which covered the Ge concentration range of interest in this study. Pure bulk Ge was also studied as a reference material. For all but the last two samples, the Raman spectrum was quite weak in the region of the scattering due to Ge type modes (∼300 cm $^{-1}$), as can be seen from Figure 6. The three major peaks observed at ∼300, ∼400, and ∼500 cm^{-1} arise from the Ge-Ge, Si-Ge, and Si-Si modes of the alloy layer(s), while the peak at 520 cm^{-1} is due to the Si layer(s) and/or Si substrate.[39] The dominance of the Si type modes, clearly visible in Figure 6, is a result of the Raman excitation conditions.

To obtain more detailed information about the structure of the strong peaks and the location of the weak Raman peak expected near 300 cm^{-1} for the Ge nanostructures, the spectra were curve re-

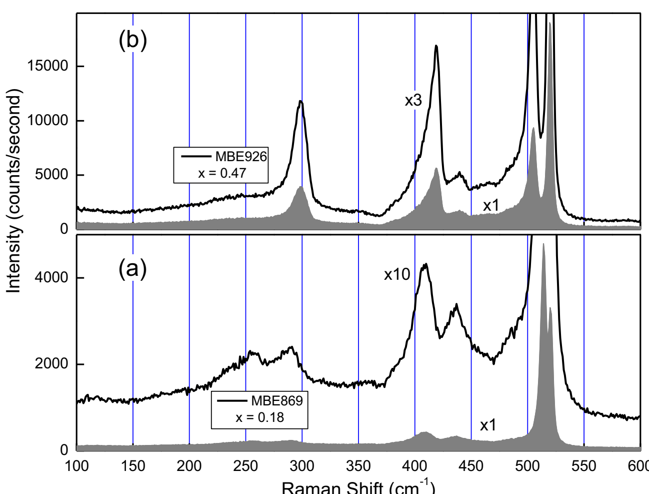

Figure 6. As-measured (raw) Raman spectra obtained at room temperature from (a) sample 869 ($x = 0.18$) and (b) sample 926 ($x = 0.47$). In both panels a vertical scale expansion has been applied to provide more detail of the weaker features of special interest in the 150 to 350 cm^{-1} range.

solved using a combined Gaussian-Lorentzian (G-L) lineshape for most peaks, an extended modified Gaussian (EMG) lineshape for the Ge-Ge mode that accounts for its asymmetry,[40] and a pure Gaussian lineshape for the Ge nanostructure mode, which also fits well to the case of bulk Ge. The fitting procedure was as follows: a number of G-L lines (ranging from 2–5, depending on the Ge concentration) plus the EMG line were fitted first to account for all major features in the Raman spectrum and then the G line was included for a final fit. Representative results obtained from the fits are shown in Figure 7 and Figure 8. In the case of the lower Ge concentration samples, a five point averaging procedure was applied to reduce the noise level in the spectrum (compare, for example, the Raman spectra in Figure 6a and Figure 7). This data smoothing greatly improved the overall quality of the fits.

The 150–350 wavenumber spectral region contains three types of contributions to the vibrational Raman spectrum. A well-defined peak

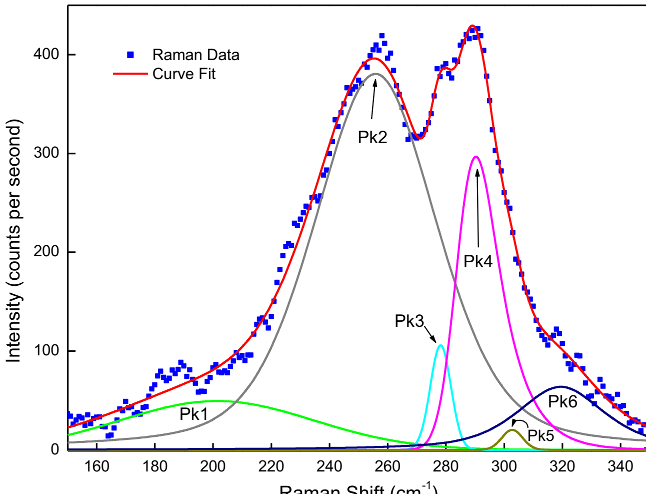

Figure 7. Curve resolved Raman spectrum of sample 346 ($x = 0.17$) at room temperature. The Raman data has been smoothed by a five point averaging procedure. The peaks labeled with the prefix "Pk" have the following forms: peaks 1, 2, 3, and 6 are combined Gaussian-Lorentzian functions, peak 5 is a Gaussian function, and peak 4 follows an extended modified Gaussian (EMG) function.

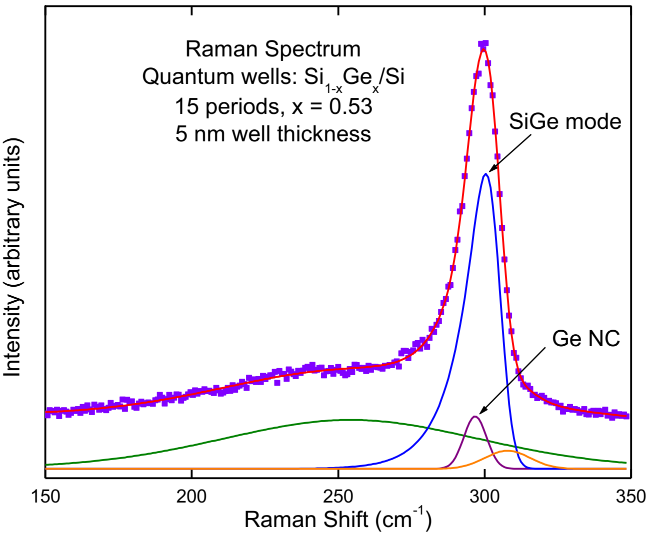

Figure 8. Room temperature Raman spectrum of a 15 period $Si_{1-x}Ge_x/Si$ multiple quantum well sample (931) with x = 0.53 and well thickness of 5 nm in the frequency region of Ge-type lattice vibrations (solid points). The spectrum has been curve resolved into the components shown underneath the fitted curve (solid line).

at about 300 cm^{-1} due to the Ge-Ge mode of the SiGe alloy, a weak sharp peak due to the Ge nanostructures, and a continuum of second-order scattering exhibiting varying degrees of structure depending on the Ge concentration in the alloy. For example, only two or three G-Ls may be needed to account for the continuum, as shown in Figure 7 and Figure 8. In other cases four or five such bands were needed. In all cases another band was required at ~310–320 cm^{-1} to account for the high wavenumber end of the scattering. In the discussion that follows we focus on the peaks observed in the 300 cm^{-1} region.

The concentration dependence of the fitted Ge-Ge and Ge mode frequencies are shown in Figure 9. These data are consistent with the results of an earlier study.[39] The existence of a sharp, although weak, Ge line in all spectra confirms the presence of Ge NCs in all of the samples studied by Raman spectroscopy. The approximately linear

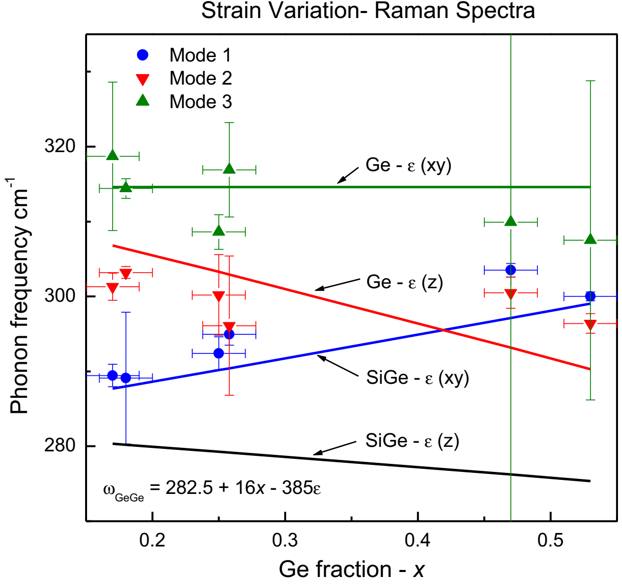

Figure 9. Concentration dependence of the zone-center Ge-Ge phonon mode frequencies, obtained from Raman scattering. For example, the blue points correspond to a Ge-Ge mode in the $Si_{1-x}Ge_x$.

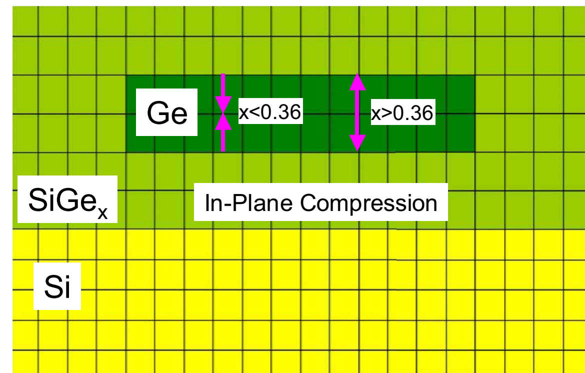

Figure 10. Cross sectional schematic for the x-z plane of lattice matched Ge NCs within SiGe on Si(001).

shift in frequency with x is a result of the strain in the alloy layer in the sample growth (z) direction, which is the primary direction of phonon propagation sampled in the Raman back-scattering experiment.

The Raman behavior can be modelled.[41] For example, we show in Figure 8 the Raman spectrum of a 15 period $Si_{1-x}Ge_x/Si$ multiple quantum well sample with x = 0.53 and an alloy layer thickness of 5 nm. The vertical tensile strain in an imbedded Ge NC would be 2.2% in this sample. The spectrum is readily curve-resolved into just four peaks. The strong asymmetric (Gaussian) sharp peak at 300.0 cm^{-1} is due to the Ge-Ge type vibrational mode associated with the strained alloy epilayer,[9] while the weaker sharp Gaussian band at 296.4 cm^{-1} is typical of Ge.[9] As reported previously,[42] this amount of uniaxial strain in a Ge nanobridge gave rise to a Raman peak at 297.0 cm^{-1}, which is quite near the value obtained here for the Ge NCs. The very broad band at 254 cm^{-1} is needed to account for a continuum of second-order Raman scattering from phonons in the epilayer, while the very weak peak at 307 cm^{-1} is needed to account for the tail of the Raman spectrum at higher frequency. The existence of the weak band at 296.4 cm^{-1} confirms the presence of Ge NCs in the SiGe epilayer and indicates that they are under tensile strain, as its frequency lies below that of bulk (unstrained) Ge (~300 cm^{-1}).

The third feature of interest varies from 308 to 320 cm^{-1} with no apparent consistent dependence on x, as can be seen in Figure 9. This feature could also arise in part from second-order Raman scattering, but it certainly contains a contribution from the Ge nanostructures. This is because the Ge nanostructure vibrations in the x-y plane, which are predicted to occur at ~315 cm^{-1} independent of x since the strained alloy layer is always lattice-matched to Si (see later discussion), could also be observed, albeit weakly, in the quasi back-scattering geometry employed here.

Consequences of lattice Matching: self-assembled Ge nanocrystals.—An examination of the available experimental evidence indicates that a possible cause of the broad peak is imbedded Ge NCs within the SiGe layers (see Figure 10). The formation of such NCs was shown in transmission electron microscopy (TEM) studies[23] (Figure 2) and by Raman spectroscopy, as discussed above. We now proceed assuming the presence of such NCs while deducing their impact in the PL and Raman results.

Referring to Figure 10, we see that ideal epitaxial growth means that the SiGe epilayers and the Ge NCs be lattice matched to Si (001) in the x-y plane, so that both the SiGe and NCs are under compression in that plane. However, the growth of SiGe is unconstrained in the vertical (z) direction. As is well known, the SiGe epilayer is under tensile strain in this direction, leading to a vertical lattice constant that increases with Ge fraction and is larger than that for unstrained SiGe. Here the volume of the unit cell for the epitaxial SiGe layer is assumed to be the same as that for unstrained cubic (bulk) SiGe. An important assumption is that the lattice constant of the Ge NCs matches that of the SiGe in all three directions, i.e., including vertically. For relatively

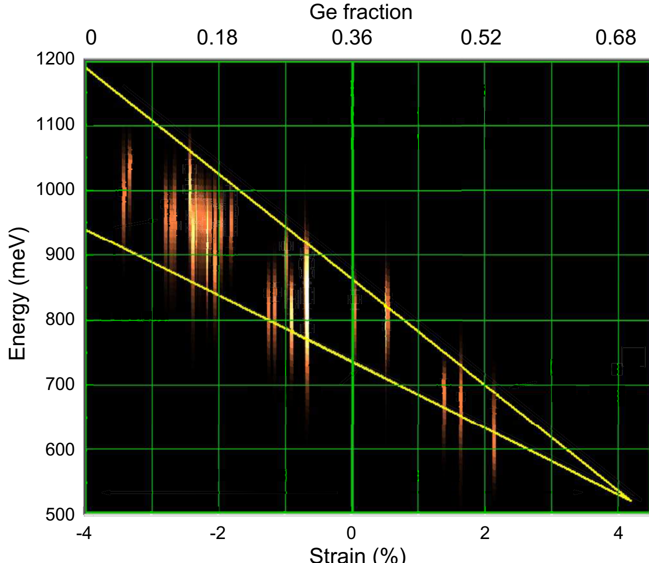

Figure 11. PL energy distributions for the broad PL versus the uniaxial vertical strain in the Ge NCs assumed to be present in the $Si_{1-x}Ge_x$ layers. The upper and lower solid lines are the direct and indirect bandgap energies for Ge calculated using deformation theory for uniaxial strain. The top horizontal scale is Ge fraction (x) from which the bottom scale strain values are derived using Equation 1.

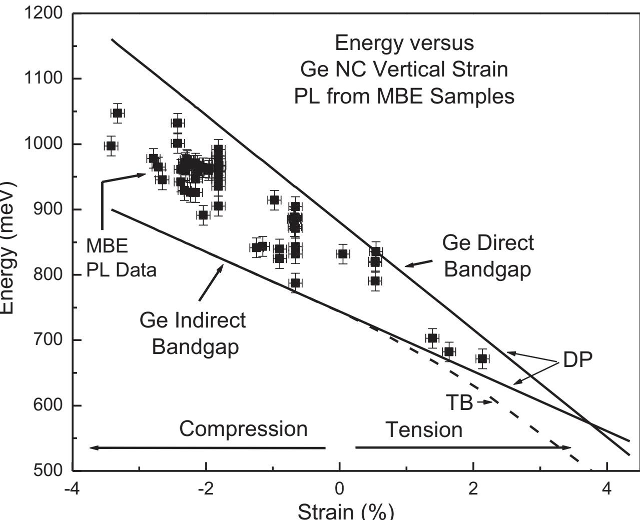

Figure 12. PL NP peak energy and bandgap (direct and indirect) energies of Ge versus Ge NC vertical strain. For the indirect gap under tensile strain, the energy has been calculated using both the DP and TB theories.

dilute SiGe, the Ge NCs are under compression vertically, but for increasing Ge content in the SiGe epilayer the vertical lattice constant of the strained SiGe eventually exceeds that of bulk Ge. At the point where the vertical strain in the Ge NC first becomes tensile, the Ge fraction in the SiGe is 0.36 (Figure 11). With these constraints we can write down an expression for the strain in the z direction within the Ge NCs as:

$$\epsilon_z = \left(l_c^{Ge} - l_c^{SiGez}\right) / l_c^{Ge} \qquad [1]$$

where l_c^{Ge} is the bulk Ge lattice constant (5.658 Å) and l_c^{SiGez} is the strained lattice constant in the vertical direction for tetragonally distorted SiGe material, which is lattice matched to Si in the horizontal plane. Note that the strain value is negative for compression and positive for tension. With increasing x, this lattice constant varies from 5.431 to 6.141 Å as given by the following expression:

$$l_c^{SiGez} = \left(l_c^{SiGeu}\right)^3 / \left(l_c^{Si}\right)^2 \qquad [2]$$

where l_c^{Si} is the lattice constant for Si (5.431 Å). Here l_c^{SiGeu} is the lattice constant for cubic (unstrained) SiGe given by:

$$l_c^{SiGeu} = l_c^{Si} + c_1 x + c_2 x^2 \qquad [3]$$

where x is the Ge fraction. In this quadratic equation, the symbols, c_1 and c_2, represent constants equal to 0.2 and 0.027, respectively.[43] Strain versus Ge-fraction is thus easily derived for the vertical direction as shown by the horizontal scales at the top and bottom of the graph in Figure 11.

Raman frequency variation with strain.—From Chen et al.,[41] the Ge-Ge phonon mode frequency in SiGe, as seen by Raman scattering, depends on the germanium fraction x and strain ϵ as follows:

$$\omega_{Ge-Ge} = 282.5 + 16x - 385\epsilon. \qquad [4]$$

For the Ge NCs, x is equal to unity. In the vertical direction the relevant strain, ϵ_z, for the NCs is given by Equation 1, leading to the red line in Figure 9, in which the phonon frequency declines from 312 to 290 cm^{-1} as x increases from 0.1 to 0.55. In the x-y plane the NC strain is compressive and constant at −4.18%, because the NCs are lattice matched to Si in this plane. Hence in the x-y plane, the NC Raman frequency is not expected to vary with Ge fraction in the surrounding SiGe, as shown by the green horizontal line at a Raman frequency of 314.6 cm^{-1} (calculated as per Equation 4) in Figure 9.

In the x-y plane for the SiGe layers, the increasingly compressive strain causes the Ge-Ge Raman mode frequency to rise with Ge fraction, as is apparent for the blue line in Figure 9 for which the frequency goes up from 285 to 300 cm^{-1} when the Ge fraction changes from 0.1 to 0.55. In the vertical (z) direction the strain is tensile in the SiGe layers and increases with Ge fraction, which progressively suppresses the Ge-Ge phonon mode frequency, as seen in the black line below 280 cm^{-1} in Figure 9.

The theoretical predictions are in general agreement with experiment, as can be seen in Figure 9.

Bandgap variation with strain.—Strain has a relatively large effect on material bandgap energy, with compression generally increasing this energy while tension reduces it. A relatively simple method for calculating this effect is to use deformation potential (DP) theory, which employs linear relationships between strain and the direct and indirect bandgaps, as per:

$$E_{BG} = A + B \times \epsilon_z \qquad [5]$$

Here, for strain expressed in per cent, the intercept and slope in the linear equation are 880 and −79.3 meV for the direct bandgap and 740 and −45.5 meV for the indirect one at low temperatures.[44] For example, for a tensile strain of 2%, the direct BG energy is 721 meV and the indirect BG is 649 meV.

From DP theory, as the strain becomes more strongly tensile both the direct and indirect gap energies decline, with the direct energy decreasing more rapidly than the indirect one. As shown in Figure 12, the direct gap energy crosses over the indirect gap energy at a tensile uniaxial strain of 4%, resulting in Ge becoming a direct gap semiconductor, a highly desirable outcome. Our results with PL point the way to this transition point, but the maximum vertical tensile strain for the present Ge NCs is not much greater than 2%. Nonetheless, the fact that we see PL below the indirect BG of bulk Ge is explained by these particular Ge NCs being under tensile strain vertically, which reduces their Ge BG. As discussed later, there are other models for the bandgap energy such as tight binding (TB),[44] for which Figure 12 contains the indirect bandgap calculation under tensile strain.

For the bandgap curves calculated versus strain in Figure 12 the effects of quantum confinement have not been included. The data points were obtained by curve resolving the PL of the MBE-grown SiGe

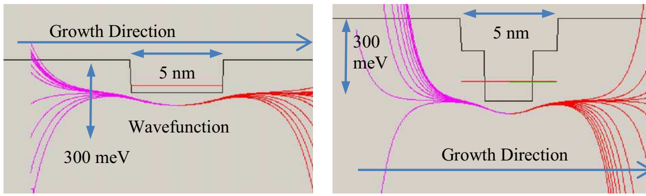

Figure 13. Shooting method results for calculating the bound exciton energy in a single well (left) SiGe/Si layered system and a double well (right) Ge-SiGe/Si layered system. The left panel depicts the result for a $Si_{0.85}Ge_{0.15}$ quantum well 5 nm thick. On the right, a 2.5 nm thick Ge NC has been added in the middle of the original SiGe well, which resulted in a reduction of the lowest bound exciton energy by 130 meV compared with the single well case.

samples. In Figure 12 the points are Ge NC NP PL peak energies and the solid lines are the direct and indirect NC BGs (Equation 5). The NP experimental peak energies have been obtained from the broad PL distributions depicted in Figure 11 by fitting Gaussian functions to the observed PL spectra. In Figure 12 and in Figure 11 we note that the data falls generally above the indirect energy BG for uniaxially strained Ge, a differential which is most likely due to quantum confinement, as will be discussed next. This is a difference that appears to decrease as compression decreases, although there are only a few points for the larger tensile strains. The energy uncertainties in the data points are those obtained from curve resolving the PL peaks. The strain uncertainties for these points are derived from the X-ray diffraction measurements of the composition and thickness of the SiGe layers. Figure 11 shows the color-weighted actual distributions in energy for the broad NC PL peaks, versus vertical NC strain. For a number of the strain values, there are several samples for which the PL spectra overlap giving rise to composite distributions that appear to be relatively intense.

Calculation of bound exciton energy for Ge NCs.—To test the NC hypothesis further, we have calculated the emission energy in a simple numerical model that accounts for the effects of strain on the Ge BG and of the confinement blue shifts in the exciton PL spectra for both the SiGe layers and the imbedded NCs, with the latter of a single size (2.5 nm high in the growth direction). In this model, the vertical direction is assumed to provide the lowest energy BG. We used a double well structure, consisting of both Ge and SiGe wells, with the smaller Ge wells completely imbedded in SiGe, as illustrated in Figure 10. In such a system there are related confinement shifts in both the Ge NCs and the SiGe material. While the SiGe layer thicknesses were obtained from structural measurements, as discussed previously, the NC height is not known and can be treated as somewhat of a free variable. In the formulation, we incorporate the effect of vertical strain on the NC BG first using a DP approach and later with TB theory.

Figure 13 depicts the shooting method[45] used in calculating the bound exciton energy in the double well Ge-SiGe/Si layered system. The shooting method is used for solving one-dimension Schrodinger-type equations for the bound energy with arbitrary potentials. Here we choose an initial exciton energy and, using finite differences, numerically calculate the wave function throughout a layered system. This wave function calculation is extended to distances far from the starting point. If we have chosen the correct energy, the wave function will go to zero for large distances, otherwise it will diverge and we must try another energy. The left panel in Figure 13 shows the result for a $Si_{0.85}Ge_{0.15}$ quantum well 5 nm thick where the exciton energy obtained is approximately 1054 meV. On the right, a 2.5 nm strained Ge NC has been added. The lowest bound exciton energy in that case is 924 meV. The background energy is that of substrate bound excitons in silicon (1150 meV). The well structure shown illustrates the reduction in that energy due to the presence of Ge in the SiGe alloy layer and/or in the Ge NC. The horizontal lines in the quantum wells represent the energy solutions, obtained when the wavefunction is well behaved (goes to zero) far away from the quantum well in the growth direction. The exciton energy is of primary importance as it is the quantity that PL measures. The goal here is to compare this calculated no-phonon energy, which contains the confinement and strain BG shifts as well as exciton binding energies, to the observed PL energy.

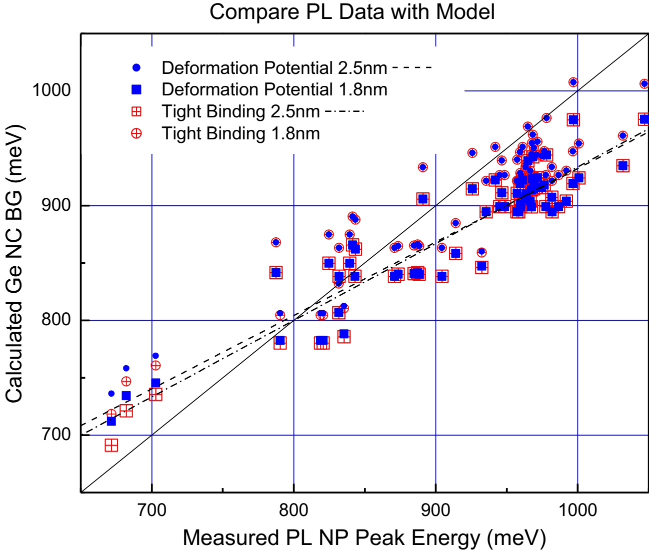

Figure 14. Theory versus experiment for the Ge NC PL from SiGe samples with Ge fractions from 0.05 to 0.53. Calculated energies for two BG models (DP and TB) for all samples and two NC sizes (1.8 and 2.5 nm). These results are plotted versus the measured NP energies obtained from the least squares fits of Gaussian peaks to the experimental PL data. Note that, for samples in which the Ge NCs are under compression vertically, the DP theory and TB model give identical results for the strained bandgap. The solid line has a slope of unity indicating where there would be exact agreement between experimental and calculated energies. The dashed line represents the best linear fit to the DP results for 2.5 nm NCs and the dot-dash line is the fit for TB.

Comparison of calculated Ge NC energy with measured PL peak energy.—The calculated energies for the samples of varying composition are compared with the measured PL energies in Figure 14. Here for the solid square points we have used a constant NC vertical size of 2.5 nm. In Figure 14, the best-fit straight line for this size (shown by the dashed line) to the data is expected to have a slope near unity (the solid line in the figure) but is somewhat different from that value due to what are possibly lower order influences, such as variations in the NC size and deviations from the linear DP model for the strained BG. However, we do have good general agreement between our computed emission energies and those observed in PL, which provides reasonable validation for our hypothesis that imbedded Ge NCs have given rise to the intense, broad PL observed in MBE grown SiGe.

Figure 14 compares theoretical and experimental energies for Ge NC PL from SiGe samples with Ge fractions from 0.05 to 0.53. The dashed straight line is linear least-squares fit to the results for the 2.5 nm NCs with the DP model and the dot-dash line is the similar fit for the TB model. We note the two bandgap models do not give very different results in this respect for the range of strains available in the sample set. The solid line represents the result that would have been obtained had the measured and calculated energies been identical.

One point for discussion is whether or not confinement for a reasonable range of NC sizes can account for the PL being at the energies above the strained bulk Ge indirect BG, as we see in Figure 12. This difference is in the 50 to 150 meV range with an average of 103.4 meV. So we are asking whether such values are reasonable for quantum confinement effects in the Ge NCs. With the simple model described above we can provide an answer by calculating the size of the confinement effect versus NC size, QW thickness and composi-

tion. In general it was found that the variation of NC confinement energy with thickness of the host SiGe was not that large (< 5 meV) and the variation with Ge-fraction although larger was not a major contributor to the difference. For example, the NC confinement shift for a 1.5 nm NC in a 5 nm thick well was 110 meV for a Ge-fraction of 0.15 and 130 meV for a fraction of 0.50, everything else being equal. However, NC sizes in the range from 1 to 3 nm – corresponding to confinement energies from 120 to 50 meV – can indeed account for all the blue shifts from the predicted Ge NC BG that we see in the PL energies. This means that confinement shift provides a possible explanation for the difference seen between the measured PL energy and the NC bandgap. But it appears from the distribution of points in Figure 14 that the 2.5 nm average NC size employed might have been too large. A value nearer 1.5 nm would appear to be more reasonable, leading to the question as to what influences and/or limits this size. Growth conditions should of course be critical in this respect.

There are other assumptions in the present simple model that must be examined, including whether or not the DP model describes adequately the strain effect. Other authors have indicated that a TB model could prove to be more appropriate,[44] where for high tensile strain (> 1%) the latter model provides significantly lower indirect BGs in Ge than does the DP approach. Now we discuss the results obtained for the two models and two NC sizes (1.8 and 2.5 nm) for all the samples, illustrated in Figure 14.

After completing the calculation for two models (DPs and non-linear TB) for all the samples and the two NC sizes (1.8 and 2.5 nm), the results in Figure 14 were obtained for the calculated (vertical axis) versus measured (horizontal axis) energies. The solid line, which is for reference only, has a slope of unity and goes through the origin. In all cases the models overestimate the energy at the low end of the scale (corresponds to tensile strain) and underestimate it at the high end (compression). It appears the tensile-strained NCs are larger in the z direction than the nominal size, while the more compressed NCs are relatively smaller, with this trend skewing the curve in Figure 14.

As we see in Figure 15 the NC size trends with z-direction strain, leading to a variation in the confinement shift. We calculate this effect, to see if the sizes that we need to explain the measured-model energy difference are reasonable. As is well known the confinement shift changes with NC size such that the smaller the NC, the larger the confinement shift, etc. We have the information to compute the variation in energy shift as follows. For a given model with two NC sizes we can estimate the confinement shift per nm in this range, which averages out to be approximately 39 meV/nm and is approximately constant across the energy scale. Now if we know, for example, that a sample with PL NP energy at 672 meV and a larger calculated BE energy of 718 meV (TB at 1.8 nm) would have a size that is larger than the nominal 1.8 nm at 3.0 nm. On the other hand, another typical sample with a measured PL energy of 1047 meV but with a smaller calculated one of 1006 meV (for 1.8 nm) would be smaller than the nominal 1.8 nm at 0.8 nm: And so on. We can apply this procedure to all the samples to make the model energies equal to the measured ones. We plot the NC sizes obtained in this manner versus relative strain in Figure 15. This process results in an amplification of the scatter but we can still see the trend. When we fit this variation with a linear function, we see that the NC size varies from about 1 nm for a compressive strain of 4% to 3 nm for tensile strain of 2%.

Comparison with previous results for PL from Ge quantum dots.—Although there has been significant effort regarding Ge nanostructures,[4,46] seemingly the most relevant example of prior PL work on Ge quantum dots grown by MBE on Si (001) is that of the Stuttgart group.[7,47] In their earlier work,[47] fifty layers of C-induced Ge QDs separated by 9.6 nm thick layers of Si were studied via PL. Each dot layer consisted of 0.2 monolayer (ml) C and 2.4 mls Ge, with the C-induced dots being 10 to 15 nm in diameter and 1 to 2 nm in height. The carbon layer effectively strain compensated the germanium layer so that the Ge dots were essentially unstrained. In the later work[7] a similar structure was used, although the Ge was approximately 10% thinner at 2.2 mls. With the Ge lattice constant of 0.566 nm, 2.2 mls

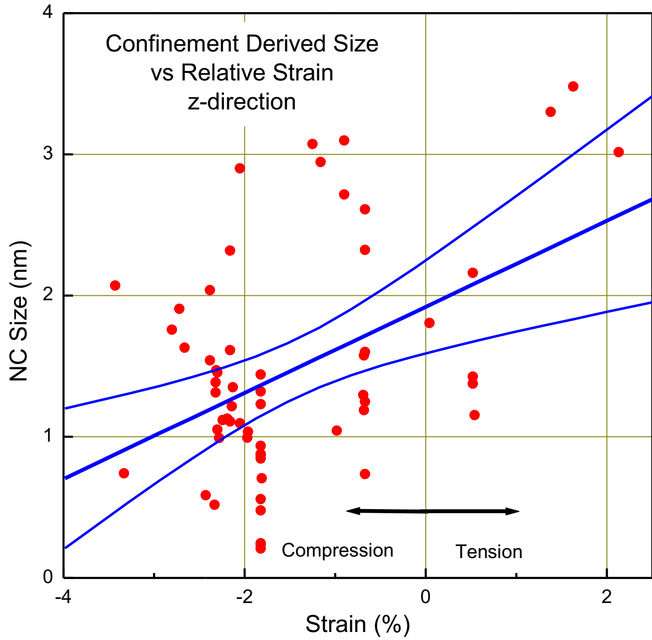

Figure 15. Confinement adjusted size is plotted versus the relative strain in the z-direction. Negative abscissa values correspond to compression in the z-direction. The size is deduced from the amount of confinement shift needed to bring the calculated exciton energy in line with the observed NP energy. The DP model results shown in Figure 14 have been used to obtain the size variation of the confinement energy (~39 meV/nm). By dividing this value into the difference between the calculated energy for a NC size of 1.8 nm and the observed NP peak energy, we obtain the amount to be added to the nominal NC size (1.8 nm) to deduce the NC size for which the theoretical energy equals that of the NP peak. The upper and lower curved blue lines correspond to the 95% upper and lower confidence bands for the linear fit.

of Ge is 1.25 nm thick and 2.4 mls is 1.36 nm thick. For 2.4 mls, the calculated confinement is about 220 meV and for 2.2 mls it is 240 meV.

In Figure 16 we show the earlier Stuttgart PL data[47] curve resolved into three Gaussian peaks. Two of the fitted peaks are associated with the NP and primarily the LA replica lines, centered at 998.2 and 967.7 meV with widths of 38.2 and 61.7 meV, respectively. Here the ratio of the integrated intensities of the NP to the phonon replica is approximately 0.9 ± 0.1. The third Gaussian compensates for the background to lower energy. The NP-PR separation here is 30.5 meV, similar to the bulk LA phonon value for Ge of approximately 28 meV. The difference in energy between the dot NP peak and the bulk Ge NP energy is approximately 258 meV, which suggests the dot height could be more like 0.99 nm, as we would expect a confinement shift in this system of approximately 215 meV for 2.4 mls (2.4 mls ~ 1.36 nm). The extra energy shift could also be due to alloying with C near the dot boundaries, which would also increase the bandgap while making the thickness of Ge smaller. If confinement were the only effect shifting the NP peak, the width of the NP peak would suggest a range of dot thicknesses from 0.7 to 1.3 nm.

The more recent Stuttgart PL data[7] was similarly fitted to three Gaussians. Two of the Gaussians were associated with the NP and LA PL lines, at 1043.1 and 1012.5 meV, respectively. A third Gaussian was used to compensate for the background to lower energy. The NP-PR separation for this sample was 30.6 meV. The difference in energy between the Ge dot NP peak and the bulk Ge NP energy was approximately 303 meV, which suggest the dot height was more like 0.61 nm instead of the designed 1.25 nm, for which we expect a confinement shift of approximately 228 meV. Again, the extra energy shift could be due to alloying with C, which would increase the bandgap and reduce the thickness of pure Ge in the dots. As the effective C to Ge ratio is larger for this sample than for the older sample,[47] we would expect the

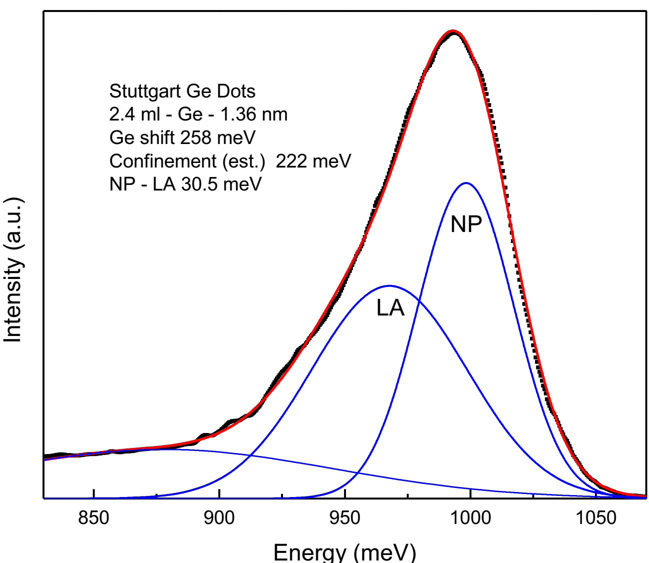

Figure 16. Least squares fit to the Ge dot PL data from Stuttgart using three Gaussian functions.

alloying shift to be larger as well, which could explain the apparent acceleration in the shift with decreasing Ge thickness. If confinement were the only effect shifting the NP peak, the width of the NP peak would suggest a range of dot thicknesses from approximately 0.45 to 0.85 nm.

We note the similarity in spectral shape of the Stuttgart dots to that for our NCs (see Figure 2 and Figure 3). The NP-PR separation (30.6 meV) is similar to, but somewhat lower than, the value (34.8 meV) that we obtain for our NCs. For momentum conserving phonons, the strongest replica for Ge is the LA one that has an energy of 27.98 meV, while relatively weak TO and TA PRs appear 36 and 10.20 meV below the NP line.[48] For Ge samples, notably doped ones, the LA replica is at least 3 times stronger than the TO replica, so that the NP-PR separation should tend toward the LA energy value for Ge, as is the case for the Stuttgart Ge dots. For dots in general, a strong NP peak is expected, due to carrier localization. Size variations in the dots lead directly to a widening of both the NP and PR resolved peaks, which are approximately 35 and 60 meV wide, respectively. We note that the low temperature PL is quite intense, as was observed for our samples. For the Stuttgart dots, a saturation effect was observed in the emission intensity versus excitation power, as we observed for our samples. Because of the presence of adjacent but extremely thin C layers, the Stuttgart dots are presumed unstrained, while ours are generally strained, although some of them have near zero vertical strain. The size of the Stuttgart dots works out to be 1.25 to 1.36 nm in the z-direction. This size is quite consistent with the range for sizes that we have deduced from confinement effects, which is 0.8 to 3.0 nm over a wide range of strain conditions, from compression through tension. In these results the vertical size corresponding to zero strain is about 1.6 nm, which is essentially equal to the Stuttgart group's estimate of "1 to 2 nm in height". The lateral diameter of the the Stuttgart dots is 10 to 15 nm. Although we have no information about the similar property for our NCs, a diameter of 10 to 15 nm would make any lateral confinement effect on the excitons relatively minor, although the $\sim$ 10 meV lateral confinement shift could account for some of the difference between the calculated 1D confinement shift and the observed shift. The confinement shifts for unstrained QDs are 257.2 meV for 1 nm and 139.3 meV for 2 nm.

To evaluate whether or not the Stuttgart dots could be made up of a GeC alloy, we note that for lattice matching to Si(001), an unstrained SiGeC alloy has the formulation,[49] $Si_{1-9.22y}Ge_{8.22y}C_y$, so that for GeC, the carbon-fraction, y, is 0.11. It has been shown[49] that such Si-lattice-matched $Ge_{0.89}C_{0.11}$ has a bandgap about 1300 eV, which is much larger than the emission energies observed for the Stuttgart Ge dot PL, which peaks at approximately 1000 meV. This very significant difference (300 meV) in energy is not greatly reduced even with the inclusion of quantum confinement effects, which strongly suggests the Stuttgart unstrained dots are not comprised of $Ge_{0.89}C_{0.11}$.

The comparison here of our results with those from Stuttgart demonstrated two things. First, that other groups with similar systems have seen the same PL as we have and, second, our interpretation explains the Stuttgart data equally well as ours.

Conclusions

In this work we have revisited the previously unsolved problem as to why strong PL can be observed in $Si/Si_{1-x}Ge_x$ quantum well samples grown by MBE at energies not only consistently below that of the $Si_{1-x}Ge_x$ BG, but in the case of high Ge concentrations even below that of the Ge BG. A detailed examination of the concentration dependence of the PL no-phonon energy revealed that the likely source of the strong PL was carrier confinement in Ge NCs that had grown by self-assembly in the $Si_{1-x}Ge_x$ epilayers. The presence of such NCs within the epilayers was confirmed from Raman spectroscopy measurements. A theoretical analysis based on a DP model revealed that strain plays a major role in determining the Ge band gap: most significantly, the NC strain along the epilayer growth direction changes from compressive to tensile at $x = 0.36$, thereby explaining the previously puzzling observation of PL at energies below that of Ge. Calculations of confinement effects on the BG energy based on a double quantum well model for 2.5 nm sized Ge NCs in $Si_{1-x}Ge_x$ epilayers on Si showed good qualitative agreement with the observed PL energy variation with x. In conclusion, our modelling of the experimental results for the concentration dependence of the PL from strained $Si_{1-x}Ge_x$ epilayers for $0.05 < x < 0.55$ has shown that the intense PL at lower energies arises from imbedded Ge NCs. Such structures show promise for use as light emitters in device applications if appropriate growths at high x values can be engineered to introduce the predicted transition to a direct bandgap within Ge NCs for x values greater than 0.65.

Acknowledgments

We thank H.J. Labbé and E. Wang for technical assistance in the Raman and PL measurements and D. Perovic for the TEM results. The Hoboken (Umicore N.V.) sample was provided by H. Buijs of ABB (Bomem). We also thank Isabelle Berbezier of CNRS Marseille for the opportunity to work with their Ge nanocrystalline samples, which provided some of the inspiration for the present work.

ORCID

N. L. Rowell https://orcid.org/0000-0001-7616-9396
D. J. Lockwood https://orcid.org/0000-0002-3001-2630

References

1. L. T. Canham, *Appl. Phys. Lett.*, **57**, 1046 (1990).
2. J.-P. Noël, N. L. Rowell, D. C. Houghton, and D. D. Perovic, *Appl. Phys. Lett.*, **57**, 1037 (1990).
3. N. L. Rowell, J.-P. Noël, D. C. Houghton, and M. Buchanan, *Appl. Phys. Lett.*, **58**, 957 (1991).
4. Y. S. Tang, C. M. Sotomayor Torres, W.-X. Ni, and G. V. Hansson, *Superlattices and Microstructures*, **20**, 505 (1996).
5. S. Fukatsu, H. Sunamura, Y. Shiraki, and S. Komiyama, *Thin Solid Films*, **321**, 65 (1998).
6. L. Tsybeskov, K. D. Hirschman, S. P. Duttagupta, M. Zacharias, P. M. Fauchet, J. P. McCaffrey, and D. J. Lockwood, *Appl. Phys. Lett.*, **72**, 43 (1998).
7. K. Eberl, O. G. Schmidt, O. Kienzle, and F. Ernst, *Thin Solid Films*, **373**, 164 (2000).
8. D. N. Lobanov, A. V. Novikov, N. V. Vostokov, Y. N. Drozdov, A. N. Yablonskiy, Z. F. Krasilnik, M. Stoffel, U. Denker, and O. G. Schmidt, *Optical Materials*, **27**, 818 (2005).
9. J.-M. Baribeau, X. Wu, N. L. Rowell, and D. J. Lockwood, *J. Phys. Condens. Matter*, **18**, R139 (2006).
10. A. Karmous, I. Berbezier, and A. Ronda, *Phys. Rev. B*, **73**, 075323 (2006).

11. N. L. Rowell, D. J. Lockwood, G. Amiard, L. Favre, A. Ronda, I. Berbezier, M. Faustini, and D. Grosso, *Journal of Nanoscience and Nanotechnology*, **11**, 9190 (2011).
12. M. H. Nayfeh, S. Rao, N. Barry, J. Therrien, G. Belomoin, A. Smith, and S. Chaieb, *Appl. Phys. Lett.*, **80**, 121 (2002).
13. L. Tsybeskov, G. F. Grom, R. Krishnan, L. Montes, P. M. Fauchet, D. Kovalev, J. Diener, V. Timoshenko, F. Koch, J. P. McCaffrey, J.-M. Baribeau, G. I. Sproule, D. J. Lockwood, Y. M. Niquet, C. Delerue, and G. Allan, *Europhys. Lett.*, **55**, 552 (2001).
14. Q. Wan, T. H. Wang, M. Zhu, and C. L. Lin, *Appl. Phys. Lett.*, **81**, 538 (2002).
15. B. V. Kamenev, G. F. Grom, D. J. Lockwood, J. P. McCaffrey, B. Laikhtman, and L. Tsybeskov, *Phys. Rev. B*, **69**, 235306 (2004).
16. Y. C. King, T.-J. King, and C. Hu, *IEEE Trans. Electron Devices*, **48**, 696 (2001).
17. Rodolfo E. Camacho-Aguilera, Yan Cai, Neil Patel, Jonathan T. Bessette, Marco Romagnoli, Lionel C. Kimerling, and Jurgen Michel, *Optics Express*, **20**, 11316 (2012).
18. Roman Koerner, Michael Oehme, Martin Gollhofer, Marc Schmid, Konrad Kostecki, Stefan Bechler, Daniel Widmann, Erich Kasper, and Joerg Schulze, *Optics Express*, **23**, 14815 (2015).
19. Jose R. Sánchez-Pérez, Cicek Boztug, Feng Chen, Faisal F. Sudradjat, Deborah M. Paskiewicz, RB Jacobson, Max G. Lagally, and Roberto Paiella, *PNAS*, **108**, 18893 (2011).
20. Jan Petykiewicz, Donguk Nam, David S. Sukhdeo, Shashank Gupta, Sonia Buckley, Alexander Y. Piggott, Jelena Vučković, and Krishna C. Saraswat, *Nano Lett.*, **16**, 2168 (2016).
21. K. Sawano, X. Xu, S. Konoshima, N. Shitara, T. Ohno, and T. Maruizumi, *ECS Transactions*, **75** (4) 191 (2016).
22. S. Wirths, R. Geiger, N. von den Driesch, G. Mussler, T. Stoica, S. Mantl, Z. Ikonic, M. Luysberg, S. Chiussi, J. M. Hartmann, H. Sigg, J. Faist, D. Buca, and D. Grützmacher, *Nature Photonics*, **9**, 88 (2015).
23. N. L. Rowell, J.-P. Noël, D. C. Houghton, A. Wang, L. C. Lenchyshyn, M. L. W. Thewalt, and D. D. Perovic, *J. Appl. Phys.*, **74**, 2790, (1993).
24. D. C. Houghton, *J. Appl. Phys.*, **70**, 2136 (1991).
25. N. L. Rowell, *Proceedings of International Conference on Raman and Luminescence Spectroscopy in Technology*, SPIE, San Diego, **822**, pp. 161 (1987).
26. D. J. Lockwood, M. W. C. Dharma-wardana, J.-M. Baribeau, and D. C. Houghton, *Phys. Rev. B*, **35**, 2243 (1987).
27. A. E. Mayer and E. C. Lightowlers, *J. Phys. C: Solid State Physics*, **12**, L539 (1979).
28. A. E. Mayer and E. C. Lightowlers, *J. Phys. C: Solid State Physics*, **12**, L945 (1979).
29. A. G. Steele and E. C. Lightowlers, *J. Phys.: Condens. Matter.*, **3**, 4491 (1991)).
30. R. R. Lieten, K. Bustillo, T. Smets, E. Simoen, J. W. Ager III, E. E. Haller, and J.-P. Locquet, *Phys. Rev.*, **B86**, 035204 (2012).
31. M. Allardt, Vl. Kolkovsky, S. Kolodinski, N. V. Abrosimov, K. Irmscher, P. Clauws, J. Weber, and K. Zuber, *Solid State Phenomena*, ISSN: 1662–9779, **178–179**, 289 (2011).
32. M. Allardt, Vl. Kolkovsky, K. Irmscher, and J. Weber, *Journal of Applied Physics*, **112**, 103701 (2012).
33. A. H. Simon, F. M. Steranka, and J. P. Wolfe, *Phys. Rev.*, **B40**, 4003 (1989).
34. P. Etchegoin, J. Weber, M. Cardona, W. L. Hansen, K. Itoh, and E. E. Haller, *Solid State Communications*, **83**, 843 (1992).
35. Landolt-Bornstein "Numerical Data and Functional Relationships in Science and Technology", Volume 17, Subvolume c, "Technology of Si, Ge and SiC", p. 102, Springer-Verlag Berlin (1984).
36. M. K. Nissen, A. G. Steele, and M. L. W. Thewalt, *Phys. Rev.*, **B41**, 7926 (1990).
37. G. Davies, *Physics Reports*, **176**, 83 (1989).
38. J. M. Feldman and K. M. Hergenrother, *J. Appl. Phys.*, **42**, 5563 (1971).
39. H. K. Shin, D. J. Lockwood, and J. M. Baribeau, *Solid State Commun.*, **114**, 505 (2000).
40. D. J. Lockwood and Z. R. Wasilewski, *Phys. Rev. B*, **70**, 155202 (2004).
41. H. Chen, Y. K. Li, C. S. Peng, H. F. Liu, Y. L. Liu, Q. Huang, J. M. Zhou, and Qi-Kun Xue, *Phys. Rev. B*, **65**, 233303 (2002).
42. A. Gassenq, S. Tardif, K. Guilloy, I. Duchemin, N. Pauc, J. M. Hartmann, D. Rouchon, J. Widiez, Y. M. Niquet, L. Milord, T. Zabel, H. Sigg, J. Faist, A. Chelnokov, F. Rieutord, V. Reboud, and V. Calvo, *J. Appl. Phys.*, **121**, 055702 (2017).
43. J. P. Dismukes, L. Ekstrom, and R. J. Paff, *J. Phys. Chem.*, **68**, 3021 (1964).
44. K. Guilloy, N. Pauc, A. Gassenq, Y. M. Niquet, J. M. Escalante, I. Duchemin, S. Tardif, G. Osvaldo Dias, D. Rouchon, J. Widiez, J. M. Hartmann, R. Geiger, T. Zabel, H. Sigg, J. Faist, A. Chelnokov, V. Reboud, and V. Calvo, *ACS Photonics*, **3**, 1907 (2016).
45. J. R. Merrill, p. 191, "Using Computers in Physics", Houghton Mifflin, Boston, ISBN 0-395-21411-4 (1976). W. H. Press, S. A. Teukolsky, W. T. Vetterling, and B. P. Flannery, Section 18.1, "Numerical Recipes: The Art of Scientific Computing (3rd ed.)", Cambridge University Press, New York, ISBN 978-0-521-88068-8 (2007).
46. N. L. Rowell, D. J. Lockwood, I. Berbezier, and A. Ronda, *Journal of the Electrochemical Society*, **156**, H913 (2009).
47. O. G. Schmidt, K. Eberl, S. Schieker, N. Y. Jin-Phillipp, F. Phillipp, J. Auerswald, and P. Lamperter, *Mat. Res. Soc. Symp. Proc.*, **533**, 171 (1998).
48. J. Weber and M. I. Alonso, *Phys. Rev. B*, **40**, 5683 (1989).
49. J. Kolodzey, P. R. Berger, B. A. Orner, D. Hits, F. Chen, A. Shao, M. M. Waite, S. Ismat Shah, C. P. Swann, and K. M. Unruh, *J. Cryst. Growth*, **157**, 386 (1995).